44th AIAA Aerospace Sciences Meeting and Exhibit
9 - 12 January 2006, Reno, Nevada

AIAA 2006-1108

Direct Numerical Simulation and the Theory of Receptivity in a Hypersonic Boundary Layer

Anatoli Tumin*
The University of Arizona, Tucson, AZ 85721, USA
Xiaowen Wang† and Xiaolin Zhong‡
The University of California, Los Angeles, CA 90095, USA

Direct numerical simulation of receptivity in a boundary layer over a sharp wedge of half-angle 5.3 degrees was carried out with two-dimensional perturbations introduced into the flow by periodic-in-time blowing-suction through a slot. The free stream Mach number was equal to 8. The perturbation flow field downstream from the slot was decomposed into normal modes with the help of the biorthogonal eigenfunction system. Filtered-out amplitudes of two discrete normal modes and of the fast acoustic modes are compared with the linear receptivity problem solution. The examples ilustrate how the multimode decomposition technique may serve as a tool for gaining insight into computational results.

I. Introduction

The progress being made in computational fluid dynamics provides an opportunity for reliable simulation of such complex phenomena as laminar-turbulent transition. The dynamics of flow transition depends on the instability of small perturbations excited by external sources. Computational results provide complete information about the flow field, which would be impossible to measure in real experiments. However, validation of the results might be a challenging problem. Sometimes, numerical simulations of small perturbations in boundary layers are accompanied by comparisons with results obtained within the scope of the linear stability theory. In principle, this is possible in the case of a flow possessing an unstable mode. Far downstream from the actuator, the perturbations might be dominated by the unstable mode, and one may compare the computational results for the velocity and temperature perturbation profiles and their growth rates with the linear stability theory. This analysis does not work when the amplitude of the unstable mode is comparable to that of other modes, or when one needs to evaluate the amplitude of a decaying mode.

Recently, a method of normal mode decomposition was developed for two- and three- dimensional perturbations in compressible and incompressible boundary layers.[1–3] The method is based on the expansion of solutions of linearized Navier–Stokes equations for perturbations of prescribed frequency into the normal modes of discrete and continuous spectra. The instability modes belong to the discrete spectrum, whereas the continuous spectrum is associated with vorticity, entropy, and acoustic modes. Because the problem of perturbations within the scope of the linearized Navier–Stokes equations is not self-adjoint, the eigenfunctions representing the normal modes are not orthogonal. Therefore, the eigenfunctions of the adjoint problem are involved in the computation of the normal modes' weights.

Originally, the method based on the expansion into the normal modes was used for analysis of discrete modes (Tollmien–Schlichting–like modes) only. After clarification of uncertainties associated with the continuous spectra in Ref. 1, the method was also applied to the analysis of roughness-induced perturbations.[4–6] In order to find the amplitude of a normal mode, one needs profiles of the velocity, temperature, and pressure perturbations, together with some of their streamwise derivatives given at only one station downstream from the disturbance source. Because computational results can provide all the necessary information about the perturbation field, the application of the multimode decomposition is straightforward. However, the first

*Associate Professor, Department of Aerospace and Mechanical Engineering, Associate Fellow AIAA.
†Graduate Student,Mechanical and Aerospace Engineering Department, Member AIAA.
‡Professor, Mechanical and Aerospace Engineering Department, Associate Fellow AIAA.

application of multimode decomposition was carried out for analysis of experimental data in a laminar wall jet when only one velocity component was measured.[7] The main feature of the laminar wall jet is that two unstable modes can coexist in the flow. This allowed the assumption that these modes provide the main input into the measured signal somewhere far downstream from an actuator. Therefore, the decomposition became possible with the help of one velocity component measured at a downstream station. Comparison of recovered and measured data illustrated good agreement.

In the present work, we apply the multimode decomposition method to an analysis of the direct numerical simulations of a high-speed boundary layer receptivity to wall blowing-suction, and compare the amplitudes of the modes found as a projection of the computational results with ones predicted by the linear receptivity theory.

Briefly, the structure of the paper is as follows. Setup of the direct numerical simulation and the results used in the multimode decomposition are presented in §II. A brief description of the theoretical approach is provided in §III. Decompositions of the computational results and their comparisons with the theoretical prediction are described in §IV. In §V, we discuss the results and outline their possible extensions.

II. Numerical approach

A numerical simulation was carried out by Wang and Zhong[8] to determine the receptivity of a Mach 8.0 flow over a sharp wedge to blowing-suction through a slot in the wall. The wedge had a half-angle of 5.3°. The free stream parameters were: velocity $U_\infty = 1181.7$ m/s, density $\rho_\infty = 0.0247$ kg/m^3, and temperature $T_\infty = 54.78$ K. For the simulation of steady base flow, the wall was adiabatic. When blowing-suction disturbances were enforced on the steady base flow, the isothermal temperature condition, which is a standard boundary condition for theoretical and numerical studies of high frequency disturbances, was applied on the wall.

The Mach 8 flow was assumed to be thermally and calorically perfect. The governing equations for the simulation were the two-dimensional Navier-Stokes equations in the conservative form, i.e.,

$$\frac{\partial \mathbf{U}}{\partial t} + \frac{\partial}{\partial x_1}(\mathbf{F}_{1i} + \mathbf{F}_{1v}) + \frac{\partial}{\partial x_2}(\mathbf{F}_{2i} + \mathbf{F}_{2v}) = 0, \tag{1}$$

where $\mathbf{U}$ is a vector containing the conservative variables of mass, momentum, and energy; $\mathbf{F}_{1i}$ and $\mathbf{F}_{2i}$ are inviscid flux vectors; and $\mathbf{F}_{1v}$ and $\mathbf{F}_{2v}$ are viscous flux vectors. Flux vectors can be expressed as

$$\mathbf{F}_{ji} = \begin{bmatrix} \rho u_j \\ \rho u_1 u_j + p\delta_{1j} \\ \rho u_2 u_j + p\delta_{2j} \\ u_j(e+p) \end{bmatrix}, \tag{2}$$

$$\mathbf{F}_{jv} = \begin{bmatrix} 0 \\ -\tau_{1j} \\ -\tau_{2j} \\ -\tau_{nj}u_n - \kappa\frac{\partial T}{\partial x_j} \end{bmatrix}, \tag{3}$$

with $j, n \in \{1, 2\}$. For compressible Newtonian flow, the viscous stress tensor can be written as

$$\tau_{ij} = \mu\left(\frac{\partial u_i}{\partial x_j} + \frac{\partial u_j}{\partial x_i}\right) - \frac{2}{3}\mu\frac{\partial u_n}{\partial x_n}\delta_{ij}, \tag{4}$$

for $i, j, n \in \{1, 2\}$. In the simulation, the viscosity coefficient, μ, and the heat conductivity coefficient, κ, were calculated using Sutherland's law together with a constant Prandtl number, $Pr = 0.72$.

The fifth-order shock-fitting method of Zhong[9] was used to solve the two-dimensional Navier–Stokes equations in a domain bounded by the bow shock and the wedge surface. The bow shock was treated as a boundary of the computational domain, which makes it possible for the Navier–Stokes equations to be spatially discretized by high-order finite difference methods. By using the shock-fitting method, the interaction between the blowing-suction disturbances and the bow shock was taken into account. The steady base flow was computed by solving (1) with a combination of the fifth-order shock-fitting method and a

second-order TVD method. In the leading edge region, a singular point at the tip of the wedge exists, which introduced numerical instability when the fifth-order shock-fitting method was used to simulate the flow. Therefore, the computational domain for the shock-fitting simulation started from a very short distance downstream of the leading edge. A second-order TVD method was used to simulate the steady base flow in a small region, including the leading edge, to supply inlet conditions for the shock-fitting simulation. For unsteady simulations, blowing-suction disturbances were introduced in a downstream region where the shock-fitting method was used. The coordinate x was defined as the distance measured from the tip of the wedge, whereas the coordinate y was the normal distance from the wall.

In the current study, the blowing-suction slot was simulated by the periodic-in-time boundary conditions for the perturbation of the mass flux on the wall that can be written as follows

$$\rho v = q_0 g(l) \sum_{n=1}^{15} \sin(\omega_n t), \tag{5}$$

where q_0 is an amplitude parameter and ω_n is the circular frequency of multi-frequency perturbations. In (5), $g\,(l)$ is the profile function defined as

$$g\,(l) = \begin{cases} 20.25l^5 - 35.4375l^4 + 15.1875l^2, & (l \le 1)\,; \\ -20.25\,(2-l)^5 + 35.4375\,(2-l)^4 - 15.1875\,(2-l)^2\,, & (l > 1)\,. \end{cases} \tag{6}$$

The variable l in (6) is a non-dimensional coordinate defined within the blowing-suction slot:

$$l\,(x) = \frac{2\,(x - x_i)}{(x_e - x_i)}, \qquad x_i \le x \le x_e; \tag{7}$$

where x_i and x_e are the coordinates of the leading and the trailing edges of the slot, respectively. The amplitude distribution, $g\,(l)$, is shown in figure 1. Numerical simulations revealed that there is no difference in the results if surface blowing-suction is specified by the perturbation in the y-velocity only. This is due to the fact that the weak perturbation is in the linear region. The corresponding velocity perturbation at $y = 0$ is

$$v(x,t) = v_w(x) \sum_{n=1}^{15} \sin(\omega_n t) = \frac{q_0}{\rho_{sw}} g(l) \sum_{n=1}^{15} \sin(\omega_n t), \tag{8}$$

where ρ_{sw} is density of the unperturbed flow on the wall. In the theoretical analysis presented in §III, we utilize (8) as the boundary condition simulating the actuation.

For the purpose of the multimode decomposition, fast Fourier transform of the perturbation field was carried out downstream from the slot at distance x_{data}. Seven cases with different x_i, x_e, and x_{data} were considered in the present work. The coordinates for each case are presented in table 1. Figure 2 shows an

Case	x_i (m)	x_e (m)	x_{data} (m)	$q_0 \times 10^5$ (kg/s m^4)	H (mm)
1	0.10159	0.11384	0.12784	0.125188	0.1251
2	0.40184	0.41384	0.42784	0.054453	0.2289
3	0.05184	0.06384	0.07784	0.214139	0.09764
4	0.15184	0.16384	0.17784	0.096130	0.1476
5	0.20184	0.21384	0.22784	0.080666	0.1670
6	0.25184	0.26384	0.27784	0.070759	0.1845
7	0.30184	0.031384	0.32784	0.063745	0.2004

Table 1. Coordinates of the leading, x_i, and trailing, x_e, edges of the slot; the coordinate of the station, x_{data}, where data were provided for the decomposition; the amplitude parameter q_0 in (5); and the length scales corresponding to the considered examples.

example of the streamwise velocity amplitude distributions obtained in the numerical simulation for case 1.

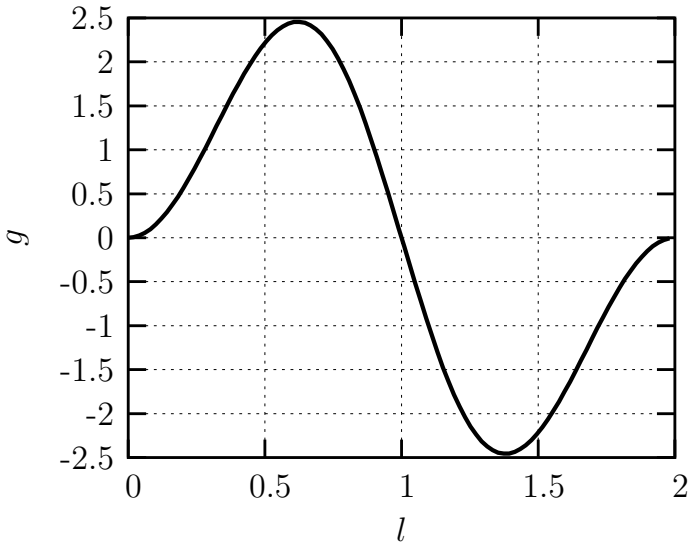

Figure 1. Amplitude distribution of the blowing-suction slot.

The velocity is scaled with the edge velocity, $U_e = 1167.3$ m/s; and the distance from the wall is scaled with $H = 0.1251$ mm.

The contours of the instantaneous pressure perturbation induced by blowing-suction disturbance at frequency 5×14.92 kHz is shown in figure 3 (case 2). After the blowing-suction slot, the excited pressure perturbations are divided into two branches: one branch penetrates the boundary layer and propagates along the Mach lines (acoustic waves) while the other branch stays within the boundary layer, which is mode S, indicated by the typical wave structures on the wall.

III. Theoretical analysis

The theoretical analysis of the numerical results includes two steps. The first one is the receptivity problem solution with the blowing-suction on the wall defined by (6). The second step is the decomposition of the perturbation field obtained in the computational part of the work into normal modes (projection onto the basis comprised of the eigenfunctions of the continuous and discrete spectra) and comparison of the found amplitudes with those predicted by the receptivity problem solution.

The multimode decomposition of two-dimensional perturbations in compressible boundary layers was introduced in Gaydos and Tumin[2] (hereafter, GT), and it can be utilized for analysis of the present problem. Alternatively, one can use the results of Ref. 3 for three-dimensional perturbations when the spanwise wavenumber, β, is very small. Similarly, the receptivity problem solution of Ref. 6 for three-dimensional perturbations introduced on the wall can be utilized for analysis of the two-dimensional problem by using $\beta \to 0$. For clarity of the method description, we recapitulate the receptivity problem solution in a form adequate for two-dimensional perturbations in a compressible boundary layer.

In the parallel flow approximation, we write down the governing equations for a two-dimensional periodic-in-time perturbation in the matrix notation of GT,

$$\frac{\partial}{\partial y}\left(\mathbf{L}_0 \frac{\partial \mathbf{A}}{\partial y}\right) + \mathbf{L}_1 \frac{\partial \mathbf{A}}{\partial y} = \mathbf{H}_1 \mathbf{A} + \mathbf{H}_2 \frac{\partial \mathbf{A}}{\partial x}, \tag{1}$$

where $\mathbf{L}_0$, $\mathbf{L}_1$, $\mathbf{H}_1$, and $\mathbf{H}_2$ are 9×9 matrices. Their non-zero elements are given in GT. Vector $\mathbf{A}$ is

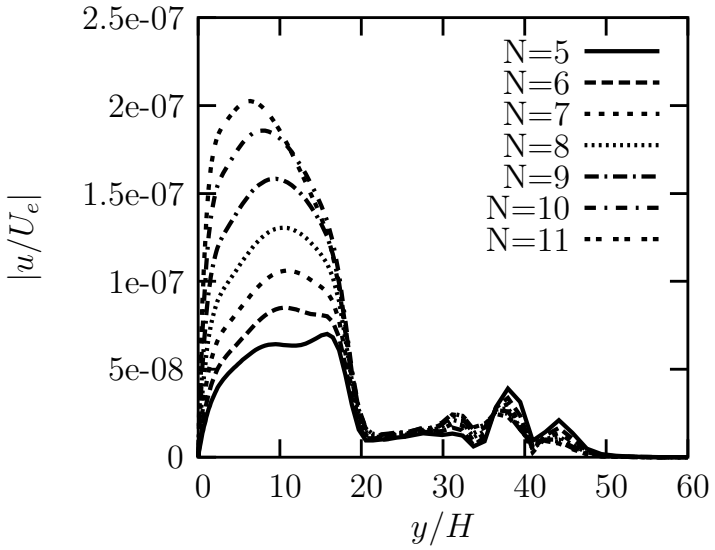

Figure 2. Amplitude distribution of the streamwise velocity component at $x = x_{data}$ and frequency $(N-1)\times 14.92$ kHz for case 1.

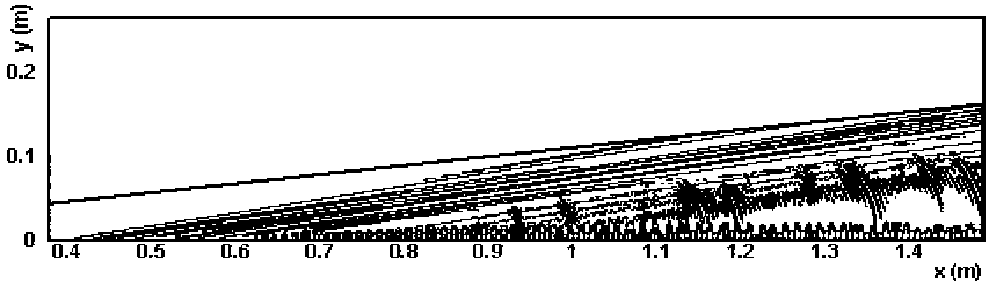

Figure 3. Contours of the instantaneous pressure perturbation induced by blowing-suction disturbance at frequency 5×14.92 kHz for case 2.

comprised of the perturbation profiles and their derivatives,

$$\mathbf{A} = \left(u, \partial u/\partial y, v, \pi, \theta, \partial\theta/\partial y,\ \partial u/\partial x, \partial v/\partial x, \partial\theta/\partial x\right)^T, \tag{2}$$

where u and v are x- and y-velocity components, respectively; π is the pressure perturbation; θ is the temperature perturbation; and T stands for transposed. In this section, the coordinate x is measured from the midpoint of the actuator. In the case of blowing-suction through a slot, the boundary conditions in the slot domain are inhomogeneous, $A_3(x,0) = v_w(x)$, and A_8 can be found from A_3 by the definition. The solution of (1) is decaying outside the boundary layer. For simplicity, we assume that the perturbation frequency is subcritical, and one can employ the Fourier transform with respect to x.

$$\mathbf{A}_v(\alpha_v, y) = \int_{-\infty}^{+\infty} \mathbf{A}(x,y)\, e^{-i\alpha_v x} dx. \tag{3}$$

In the case of a supercritical frequency, one has to refer to Briggs' method in order to include the unstable mode (exponentially growing downstream mode) into the inverse Fourier transform.[10,11]

Vector-function $\mathbf{A}_v(\alpha_v, y)$ satisfies the following equation and boundary conditions

$$\frac{d}{dy}\left(\mathbf{L}_0 \frac{d\mathbf{A}_v}{dy}\right) + \mathbf{L}_1 \frac{d\mathbf{A}_v}{dy} = \mathbf{H}_1 \mathbf{A}_v + i\alpha_v \mathbf{H}_2 \mathbf{A}_v, \tag{4}$$

$$y = 0: \quad A_{v1} = 0, \quad A_{v3} = \varphi(\alpha_v), \quad A_{v5} = 0, \tag{5a}$$
$$y \to \infty: \quad |A_{vj}| \to 0, \qquad (j = 1, ..., 9), \tag{5b}$$

where

$$\varphi(\alpha_v) = \int_{-\infty}^{+\infty} v_w(x)\, e^{-i\alpha_v x} dx. \tag{6}$$

Equation (4) has three fundamental solutions decaying outside the boundary layer. One can write down the solution of the inhomogeneous boundary-value problem as follows

$$\mathbf{A}_v = C_1 \mathbf{Z}_1 + C_3 \mathbf{Z}_3 + C_5 \mathbf{Z}_5, \tag{7}$$

where $\mathbf{Z}_1$, $\mathbf{Z}_3$, and $\mathbf{Z}_5$ are the decaying fundamental solutions. The coefficients C_j in (7) are found from the boundary conditions (5a) on the wall. The formal solution of (1) satisfying the boundary conditions can be written as follows

$$\mathbf{A}(x,y) = \frac{1}{2\pi} \int_{-\infty}^{+\infty} \mathbf{A}_v(\alpha_v, y)\, e^{i\alpha_v x} d\alpha_v. \tag{8}$$

[12] and [3] showed that the periodic-in-time solution of the linearized Navier–Stokes equations can be expanded into the normal modes of continuous and discrete spectra,

$$\mathbf{A}(x,y) = \sum_j \int_0^\infty C_j(k) \mathbf{A}_\alpha(y,k) e^{i\alpha_j(k)x} dk + \sum_m C_m \mathbf{A}_{\alpha_m}(y)\, e^{i\alpha_m x}, \tag{9}$$

where the eigenfunctions $\mathbf{A}_\alpha$ are found as solutions of the following problem:

$$\frac{d}{dy}\left(\mathbf{L}_0 \frac{d\mathbf{A}_\alpha}{dy}\right) + \mathbf{L}_1 \frac{d\mathbf{A}_\alpha}{dy} = \mathbf{H}_1 \mathbf{A}_\alpha + i\alpha \mathbf{H}_2 \mathbf{A}_\alpha, \tag{10}$$

$$y = 0: \quad A_{\alpha 1} = A_{\alpha 3} = A_{\alpha 5} = 0, \tag{11a}$$
$$y \to \infty: \quad |A_{\alpha j}| < \infty, \qquad (j = 1, ..., 9). \tag{11b}$$

The first term in (9) represents summation over the modes of the continuous spectrum (such as entropy, vorticity, and acoustic modes), and the second term represents input of the discrete modes. Vectors $\mathbf{A}_\alpha$ in (9) are solutions of the eigenvalue problem. Together with the solution of the adjoint problem, $\mathbf{B}_\alpha$,

$$\frac{d}{dy}\left(\mathbf{L}_0^T\frac{d\mathbf{B}_\alpha}{dy}\right)-\mathbf{L}_1^T\frac{d\mathbf{B}_\alpha}{dy}=\mathbf{H}_1^T\mathbf{B}_\alpha+i\alpha\mathbf{H}_2^T\mathbf{B}_\alpha, \tag{12}$$

$$y=0: \quad B_{\alpha 2}=B_{\alpha 4}=B_{\alpha 6}=0, \tag{13a}$$

$$y\to\infty: \quad |B_{\alpha j}|<\infty, \qquad (j=1,...,9), \tag{13b}$$

they represent the biorthogonal eigenfunction system $\{\mathbf{A}_\alpha,\mathbf{B}_\alpha\}$. There is the following orthogonality relation

$$\langle\mathbf{H}_2\mathbf{A}_\alpha,\mathbf{B}_{\alpha'}\rangle\equiv\sum_{j=1}^{9}\int_0^\infty\left(\mathbf{H}_2\mathbf{A}_\alpha\right)_j B_{\alpha' j}dy=Q\Delta_{\alpha,\alpha'}, \tag{14}$$

where $\Delta_{\alpha,\alpha'}$ is the Kronecker delta if α or α' belongs to the discrete spectrum, and $\Delta_{\alpha,\alpha'}=\delta(\alpha-\alpha')$ is the delta function if both α and α' belong to the continuous spectrum. The coefficient Q on the right-hand side of (14) depends on the normalization of $\mathbf{A}_\alpha(y)$ and $\mathbf{B}_\alpha(y)$.

The orthogonality relation (14) provides a tool to find coefficients C_j and C_m in the formal solution (8). With the help of the orthogonality relation (14), one can find the input of a mode for the formal solution,

$$C=\frac{\langle\mathbf{H}_2\mathbf{A},\mathbf{B}_\alpha\rangle}{Q_j}e^{-i\alpha x}. \tag{15}$$

If we consider a dot product of $\mathbf{B}_\alpha$ and (4), and integrate with respect to y over the interval $[0,\infty)$, we arrive at the following identity (we take into account explicit forms of matrices $\mathbf{L}_0$ and $\mathbf{L}_1$):

$$\begin{aligned}\left[L_0^{43}A_{v3}\frac{dB_{\alpha 4}}{dy}-A_{v3}B_{\alpha 3}\right]_{y=0}&+\left\langle\mathbf{A}_v,\frac{d}{dy}\left(\mathbf{L}_0^T\frac{d\mathbf{B}_\alpha}{dy}\right)\right\rangle\\&-\left\langle\mathbf{A}_v,\mathbf{L}_1^T\frac{d\mathbf{B}_\alpha}{dy}\right\rangle=\left\langle\mathbf{A}_v,\mathbf{H}_1^T\mathbf{B}_\alpha\right\rangle+i\alpha_v\left\langle\mathbf{A}_v,\mathbf{H}_2^T\mathbf{B}_\alpha\right\rangle,\end{aligned} \tag{16}$$

where L_0^{43} stands for the element of matrix $\mathbf{L}_0$ having indices $(4,3)$. Taking into account the adjoint equation (12), one can substitute the formal solution (8) in (15) and find with the help of (16) the following result:

$$C=\frac{1}{2\pi}\frac{1}{Q}\int_{-\infty}^{+\infty}e^{i(\alpha_v-\alpha)x}\varphi\left(\alpha_v\right)\frac{\left[L_0^{43}\frac{dB_{\alpha 4}}{dy}-B_{\alpha 3}\right]_{y=0}}{i\left(\alpha_v-\alpha\right)}d\alpha_v. \tag{17}$$

By closing the path of the integral in the upper half-plane, we find the theoretical coefficient as the residue value at the pole $\alpha_v=\alpha$:

$$C=\frac{\varphi(\alpha)}{Q(\alpha)}\left[L_0^{43}\frac{dB_{\alpha 4}}{dy}-B_{\alpha 3}\right]_{y=0}. \tag{18}$$

On the other hand, we have results of the direct numerical simulation in the form of the vector-function $\mathbf{A}_{DNS}$ at $x=x_{data}$. With the help of the orthogonality condition (14), one can find the initial amplitude, C_{DNS}, of the mode as follows:

$$C_{DNS}=\frac{\langle\mathbf{H}_2\mathbf{A}_{DNS},\mathbf{B}_\alpha\rangle}{Q(\alpha)}e^{-i\alpha x_{data}}. \tag{19}$$

Because x_{data} is close to the actuator, one can ignore the nonparallel effects in the growing/decaying of the perturbations on the interval $[0,x_{data}]$. Finally, one can compare the filtered-out coefficient C_{DNS} in (19) with the predicted C in (18).

IV. Results

A. Discrete modes

One can find details of the numerical method used for computation of the eigenvalues and eigenfunctions of the direct and adjoint problems elsewhere.[3]

Figure 4 shows the eigenvalue map corresponding to case 1 at frequency $\omega = 0.07$ ($f \approx 104$ kHz). One can see a slow (S) and a fast (F) discrete modes, and the discretized branches of the continuous spectra. There are two horizontal branches representing the slow and fast acoustic modes. Their branching points correspond to phase velocities $c = 1 \mp 1/M$, where M is the local Mach number at the edge of the boundary layer. The vertical branch is comprised of two indistinguishable at this scale branches of entropy and vorticity modes.[3] Eigenfunctions of the discrete modes decay outside the boundary layer, whereas eigenfunctions of the continuous spectra have asymptotic behavior $\sim exp(\pm iky)$ at $y \to \infty$, where k is a real parameter ($k > 0$).

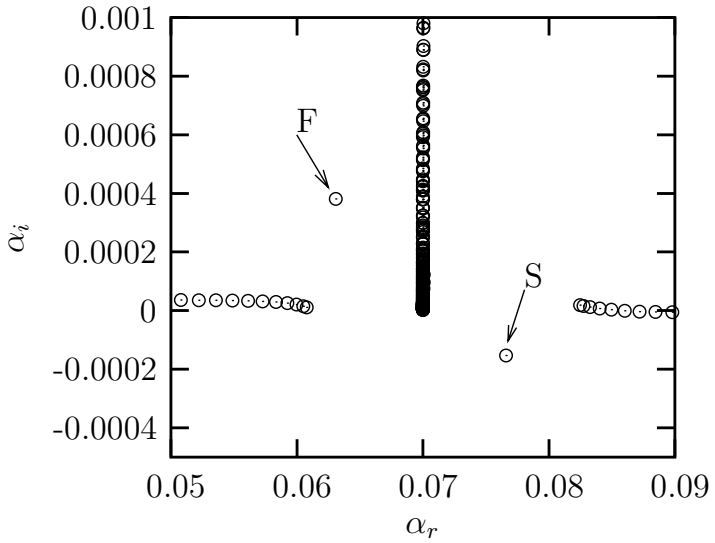

Figure 4. Eigenvalue map at $\omega = 0.07$ for case 1.

Figure 5 shows the imaginary and real parts of the wavenumber α for the discrete modes as functions of frequency, ω. Lines SA and FA in figure 5*b* represent the branching points ($k = 0$) of the slow and fast acoustic modes, respectively. One discrete mode (mode F) is synchronized with the fast acoustic mode at low frequencies, whereas the other discrete mode (mode S) is synchronized with the slow acoustic mode.

At $f \approx 150kHz$, mode F is synchronized with the vorticity and entropy modes ($c = 1$). This synchronization is accompanied by a discontinuity in α_i. As was discussed by Fedorov and Tumin,[13] the discrete mode coalesces with the continuous spectrum from one side of the branch cut and reappears on the other side at another point. Mathematically, the eigenvalue associated with mode F approaches one side of the branch cut on the complex α plane. As the pole on the plane coalesces with the branch cut, it moves to the upper Riemann sheet while, simultaneously, the pole that was on the lower Riemann sheet moves into the complex α plane at another point.

At higher frequency, $f \approx 170kHz$, there is a synchronism between mode F and mode S. However, there is no coalescence of the eigenvalues. A model of two-mode synchronism considered by Fedorov and Khokhlov[14,15] explained the branching of the modes at the point of synchronism. At this point, one of the modes becomes unstable, whereas the other one moves toward positive α_i. Although in this example the modes have the same phase velocity $c = \omega/\alpha_r$ at $f \approx 170kHz$, the minimum of $|\alpha_F - \alpha_S|$ exists in the vicinity of $f \approx 150kHz$, and, actually, this is the point where we observe the modes' branching.

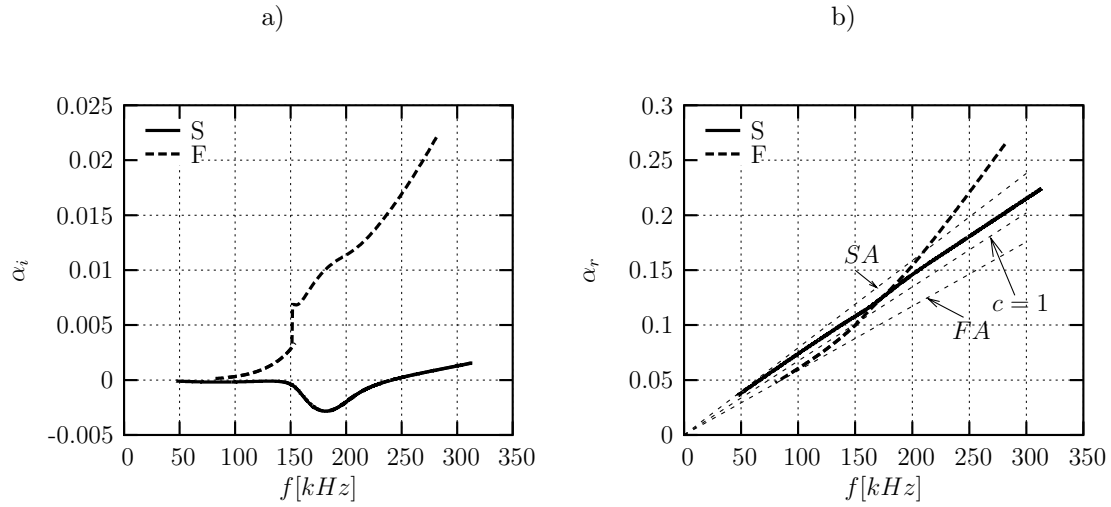

Figure 5. Imaginary (a) and real (b) parts of the wavenumber, case 1.

Both the slow and fast discrete modes could be involved in the laminar-turbulent transition scenario. For example, the decaying mode could be generated by the entropy or vorticity modes of the continuous spectra. At the point of synchronism between the fast and slow modes, the decaying mode can give rise to the unstable mode (switching of the modes), which may lead to the transition. The scenario suggested in Ref. 15 means that both the stable and unstable modes are of interest for understanding transition mechanisms. Later on, switching of the modes was observed in direct numerical simulations of perturbations in high-speed boundary layers.[16] These features of the fast and slow discrete modes explain why we need accurate simulations of the decaying mode as well.

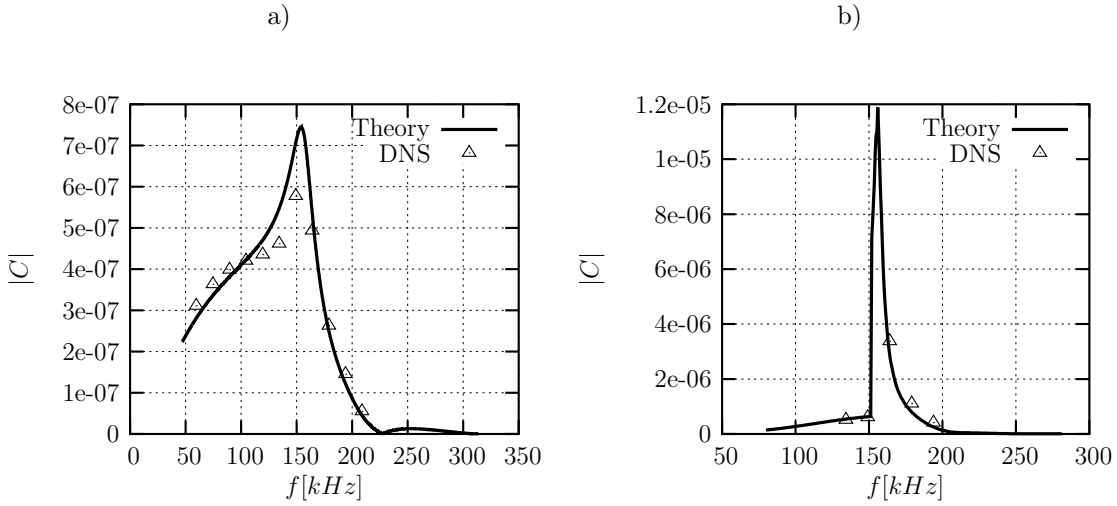

Figure 6. Comparison of the theoretical prediction for the receptivity coefficient in case 1 and comparison with data filtered out from the computational results: a) mode S and b) mode F.

Figure 6 shows a comparison of the theoretical receptivity coefficient with the amplitude filtered out from the computational results in accordance with (19). Results in figure 6 and what follows for the discrete modes correspond to normalization of the eigenfunctions when the maximum of the mass flux perturbation in the boundary layer is equal to one. Figures 7 through 12 demonstrate comparisons of theoretical and numerical results for cases 2 through 7, respectively.

One can see from the figures that there is a good agreement between amplitudes calculated with the

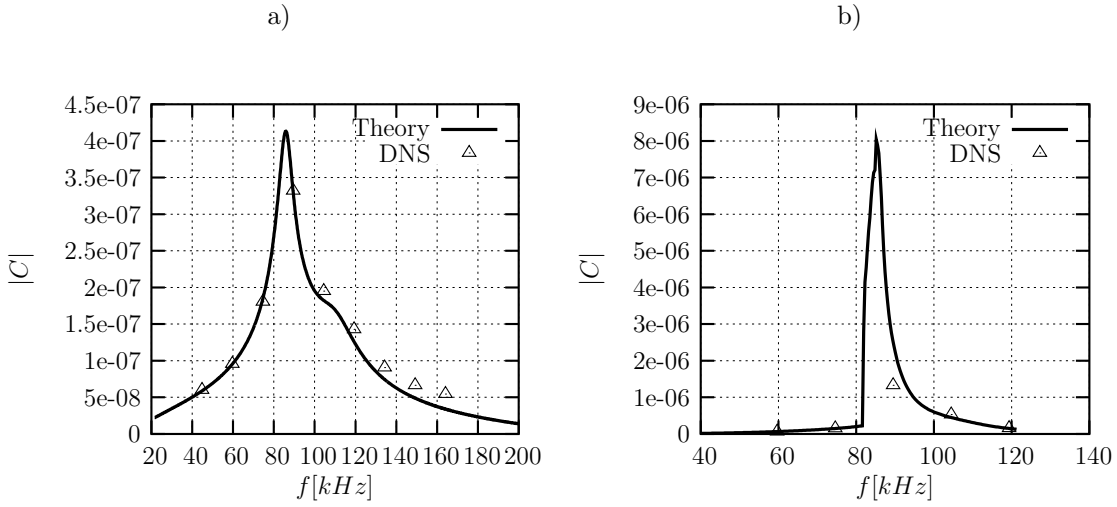

Figure 7. Comparison of the theoretical prediction for the receptivity coefficient in case 2 and comparison with data filtered out from the computational results: a) mode S and b) mode F.

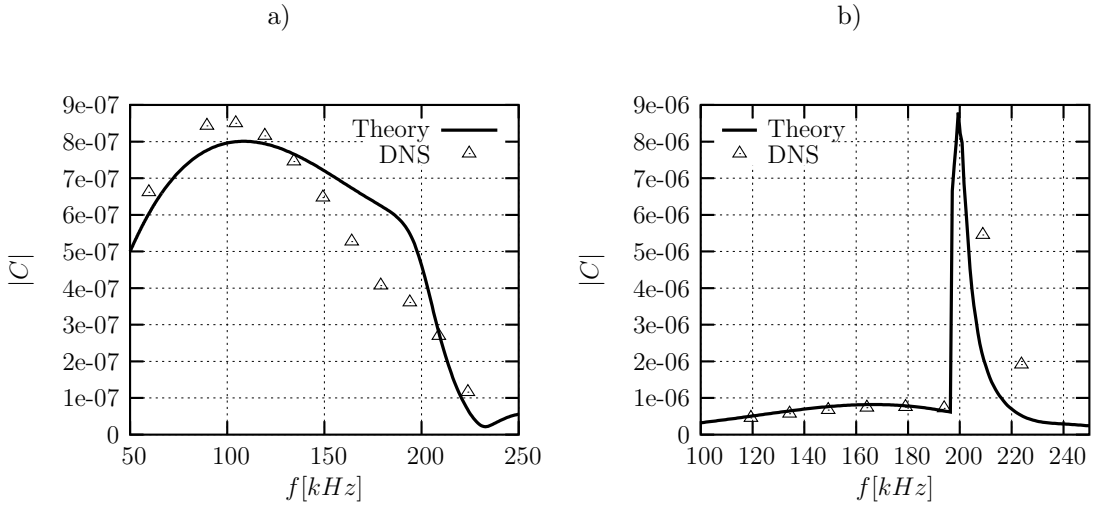

Figure 8. Comparison of the theoretical prediction for the receptivity coefficient in case 3 and comparison with data filtered out from the computational results: a) mode S and b) mode F.

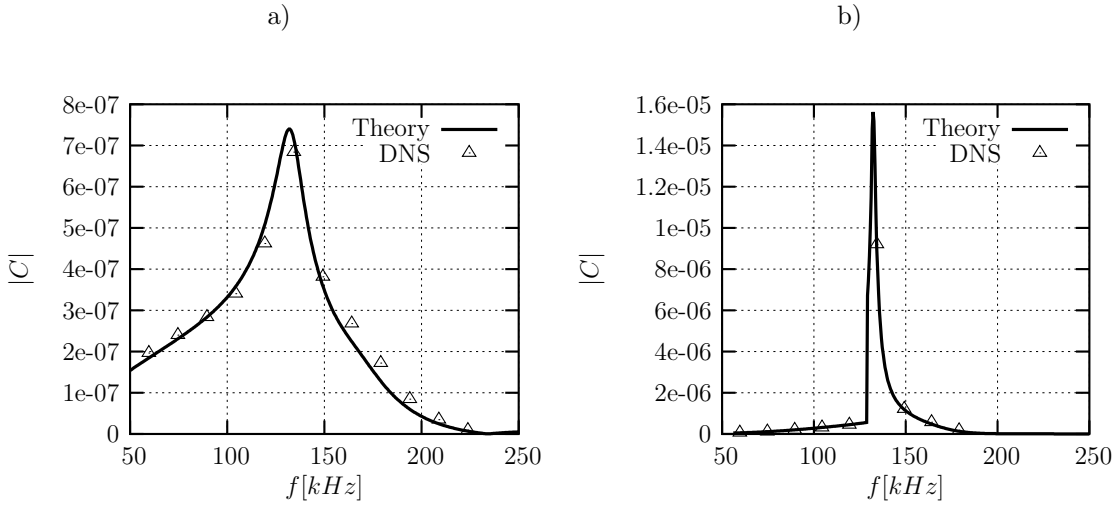

Figure 9. Comparison of the theoretical prediction for the receptivity coefficient in case 4 and comparison with data filtered out from the computational results: a) mode S and b) mode F.

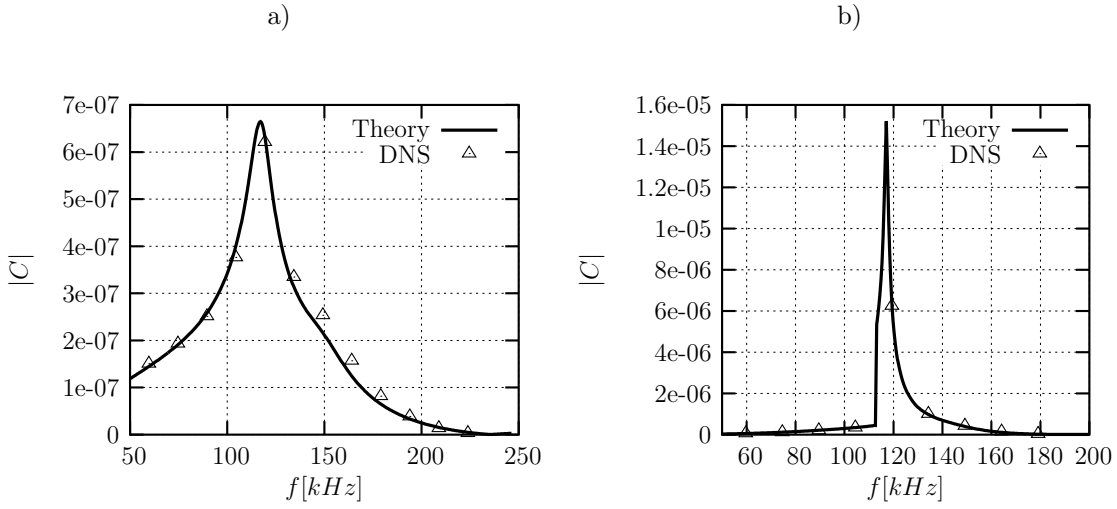

Figure 10. Comparison of the theoretical prediction for the receptivity coefficient in case 5 and comparison with data filtered out from the computational results: a) mode S and b) mode F.

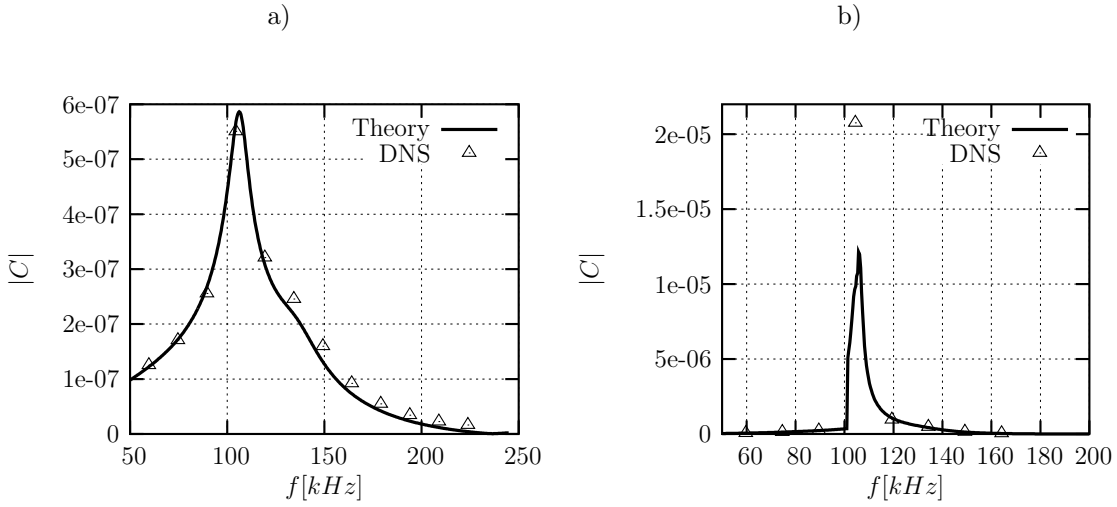

Figure 11. Comparison of the theoretical prediction for the receptivity coefficient in case 6 and comparison with data filtered out from the computational results: a) mode S and b) mode F.

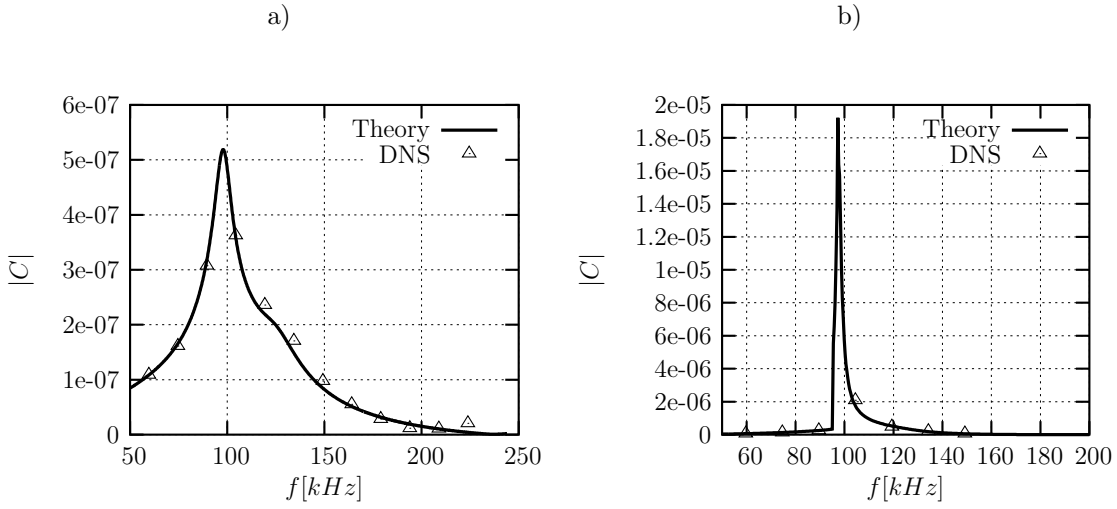

Figure 12. Comparison of the theoretical prediction for the receptivity coefficient in case 7 and comparison with data filtered out from the computational results: a) mode S and b) mode F.

help of the receptivity model of §III and those obtained from the numerical results as a projection onto the normal modes.

One can also notice that the shape of the function $|C(f)|$ for mode S in case 3 (figure 8a) is qualitatively different from the other cases, and agreement between the theoretical prediction and the numerical results is not as good. Case 3 corresponds to the closest location of the slot to the wedge's tip. The slot has a width of about 1.2 cm, whereas the distance from the tip is about 5 cm, and one should expect nonparallel flow effects, which were neglected in the present model.

The most significant discrepancy between the theory and the computational results is observed for mode F in case 6 at $f = 104.44$ kHz (figure 11b). This example corresponds to the eigenvalue located very close to the branch cut representing the vorticity/entropy modes. To illustrate qualitative difference between the mode eigenfunctions when a mode is approaching the branch cut, we show in figure 13 streamwise velocity perturbations of the neighboring discrete modes at 89.52 kHz and 119.36 kHz (phase velocities, c, of the modes in figures 13a and 13b are equal to 1.059 and 0.926, respectively). The streamwise velocity of the mode F at $f = 104.44$ kHz is shown in figure 14 ($c = 0.99$). One can see that although the amplitude of the mode decays outside the boundary layer, as it has to for a discrete mode, there are oscillations in the amplitude distribution in y typical for modes of continuous spectra. The closer the location of the eigenvalue is to the branch cut, the more similarity with the continuous spectra should be observed.

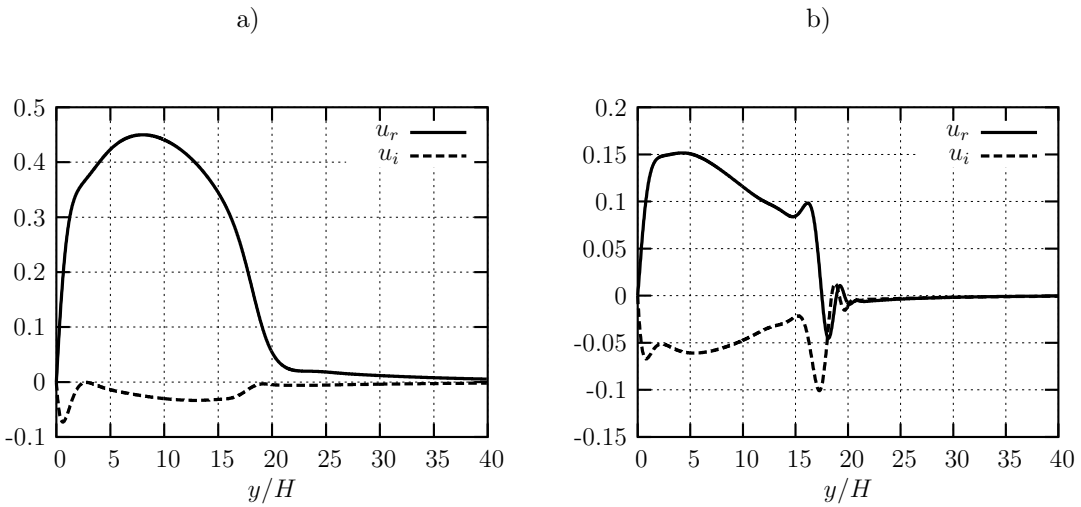

Figure 13. Streamwise velocity perturbation in discrete mode F: a) 89.52 kHz ($c = 1.059$) and b) 119.36 kHz ($c = 0.926$).

Fedorov and Khokhlov[17] considered the receptivity problem when a synchronism between two discrete modes is possible. They showed that in this case $Q = \langle \mathbf{H}_2 \mathbf{A}_\alpha, \mathbf{B}_\alpha \rangle \to 0$, and the analysis has to include both modes simultaneously, together with the nonparallel flow effects. In our example, we have a synchronism between a discrete mode and the continuous spectrum. Figure 15 shows the magnitude $|Q|$ for modes F and S as functions of frequency. One can see that in the case of mode F, Q is very close to zero at $f = 104.44$ kHz. This means that the theoretical model based on the parallel flow approximation is not adequate, and the extension of the model developed in Ref. 17 to the case of a continuous spectrum is required.

B. Acoustic modes

The biorthogonal eigenfunction expansion also provides a tool for analysis of the input from continuous spectra in the computational results. Examples of boundary layers at $M = 2$ and 4.5 considered by Balakumar and Malik[11] and by Tumin[6] indicate that input from entropy and vorticity modes due to blowing-suction through the wall is small in comparison with the acoustic modes. Therefore, we are considering the fast and slow acoustic modes only (the horizontal branches in figure 4).

Projection of the computational data onto the eigenfunction system allows evaluating the amplitudes of the modes and, therefore, revaling the underlying physics. Figure 16 shows the computational (input) data for the streamwise velocity perturbation corresponding to the frequency 134.28 kHz in case 1 at $x = x_{data}$, the

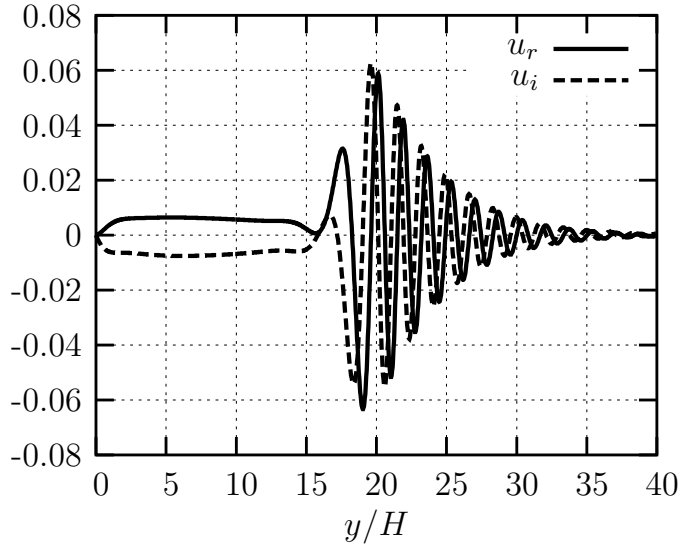

Figure 14. Streamwise velocity perturbation in discrete mode F at $f = 104.44$ kHz ($c = 0.99$).

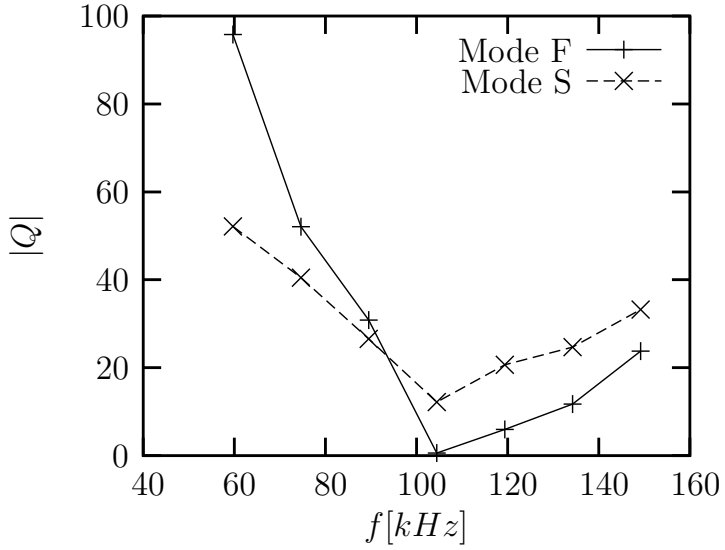

Figure 15. Magnitude of the denominator in (19),case 6.

reconstructed input of two discrete modes (S and F), and the acoustic modes ('A' stands for sum of the slow and fast acoustic modes). In this example, amplitudes of the modes were determined from the computational results with the help of the orthogonality relation (14). Integrals corresponding to the continuous spectra in (9) were evaluated numerically with respect to k from 0 to 4 with the help of the trapezoidal formula resulting from 100 steps on the interval. One can see that the acoustics provide the main input outside the

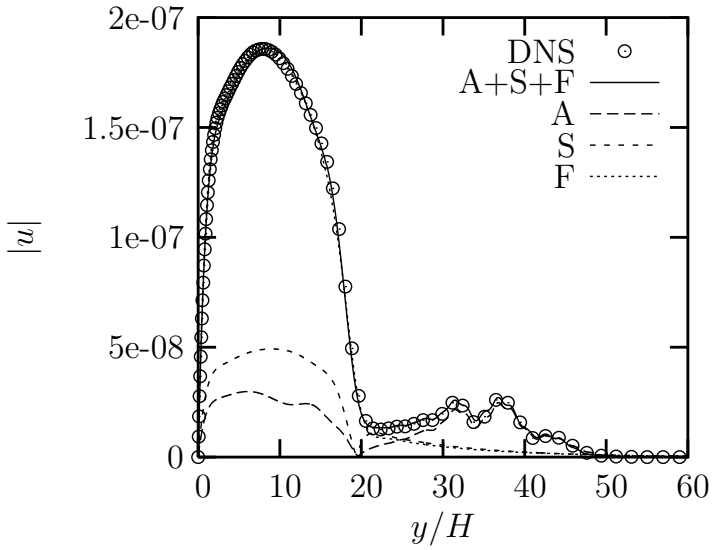

Figure 16. Input DNS data at $x = x_{data}$ and results of the projection onto modes of discrete spectrum (S and F), and the acoustic modes, case 1 (134.28 kHz).

boundary layer. The wiggles in the computational data (at $y/H \approx 35$) are associated with the Mach wave, similar to examples considered in Refs. 11 and 6. At the parameters corresponding to the results in figure 16, the main input into the perturbation profile inside the boundary layer is associated with the fast (F) discrete mode. It was also found that the slow acoustic modes have small amplitudes in comparison with the fast modes, similar to the previous studies.[6,11]

It is interesting to compare the amplitudes of the acoustic modes obtained with the help of the receptivity problem solution and their amplitudes obtained as a projection of the computational results. Figure 17*a* shows the theoretical amplitudes of the fast acoustic modes and the values filtered-out from the computational results. One can see that there is a discrepancy between them at $k \approx 1-1.5$. These values of the wavenumber correspond to a length scale of about $4-6$, which is about the step in the input data outside the boundary layer. The latter means that we need a fine grid outside the boundary layer as well, in order to evaluate the amplitudes of the acoustic modes at $k \geq 1$. Predicted velocity perturbation profiles associated with the discrete and acoustic modes are shown in figure 17*a*.

Figures 18 through 21 show comparisons of the theoretical prediction for amplitudes of the fast acoustic modes and their amplitudes found as a projection of the computational results, together with the reconstructed profiles of the velocity perturbations in case 1 at frequencies 149.2 kHz, 164.12 kHz, 179.04 kHz, and 193.96 kHz, respectively. One can see that an increase in the frequency is accompanied by an increase in the difference between the input data and the reconstructed total velocity perturbation inside the boundary layer. The discrepancy might be attributed to the appearance of higher discrete modes with the increase in the frequency, which were ignored in the present analysis.

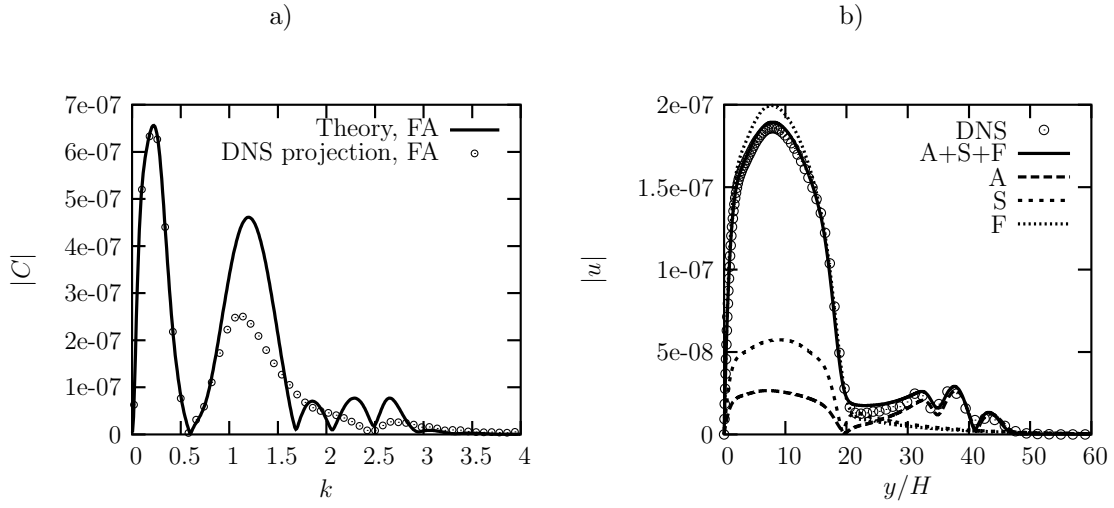

Figure 17. Amplitudes of the fast acoustic modes (a) and predicted velocity perturbation profiles (b), case 1 (134.28 kHz).

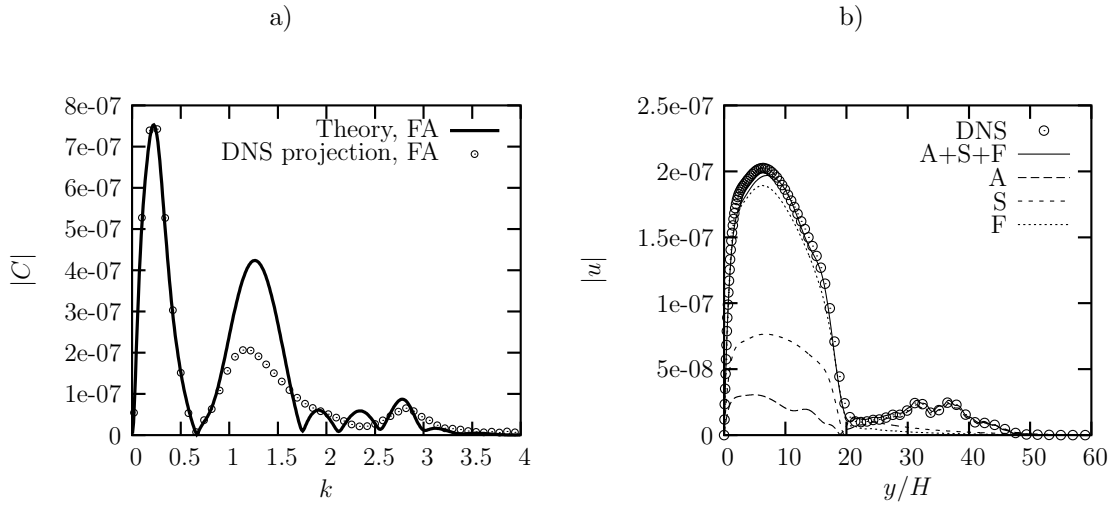

Figure 18. Amplitudes of the fast acoustic modes (a) and reconstructed velocity perturbation profiles (b), case 1 (149.2 kHz).

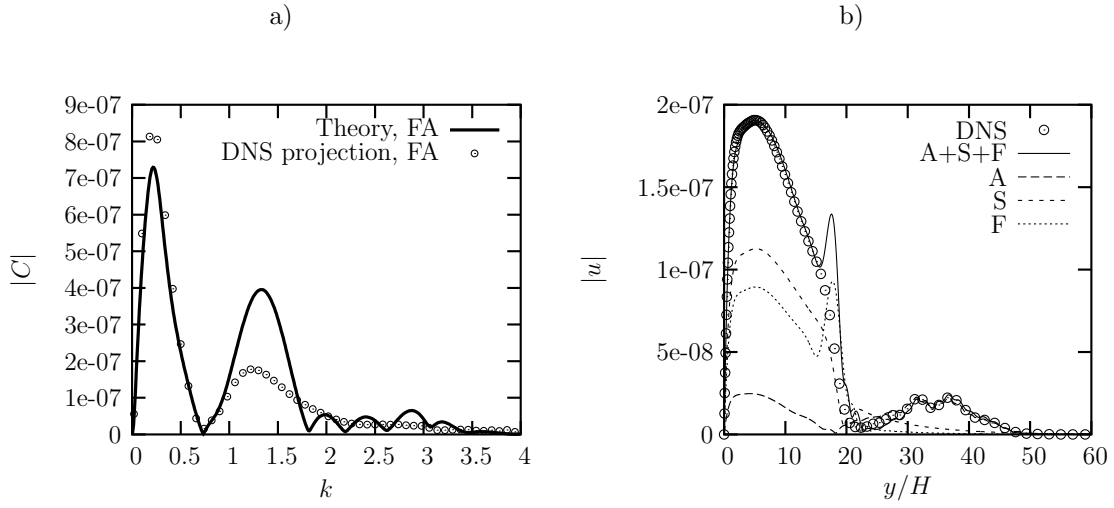

Figure 19. Amplitudes of the fast acoustic modes (a) and reconstructed velocity perturbation profiles (b), case 1 (164.12 kHz).

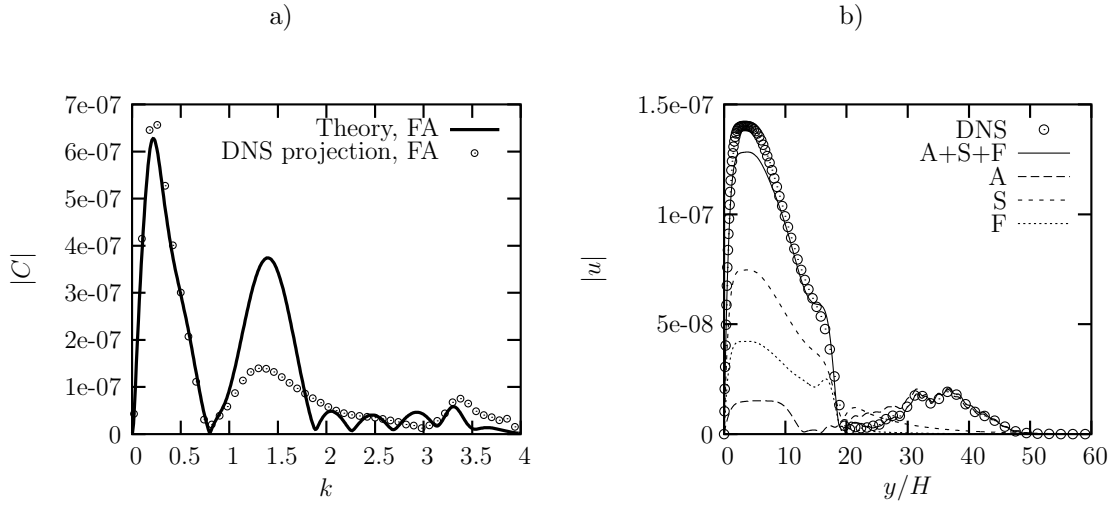

Figure 20. Amplitudes of the fast acoustic modes (a) and reconstructed velocity perturbation profiles (b), case 1 (179.04 kHz).

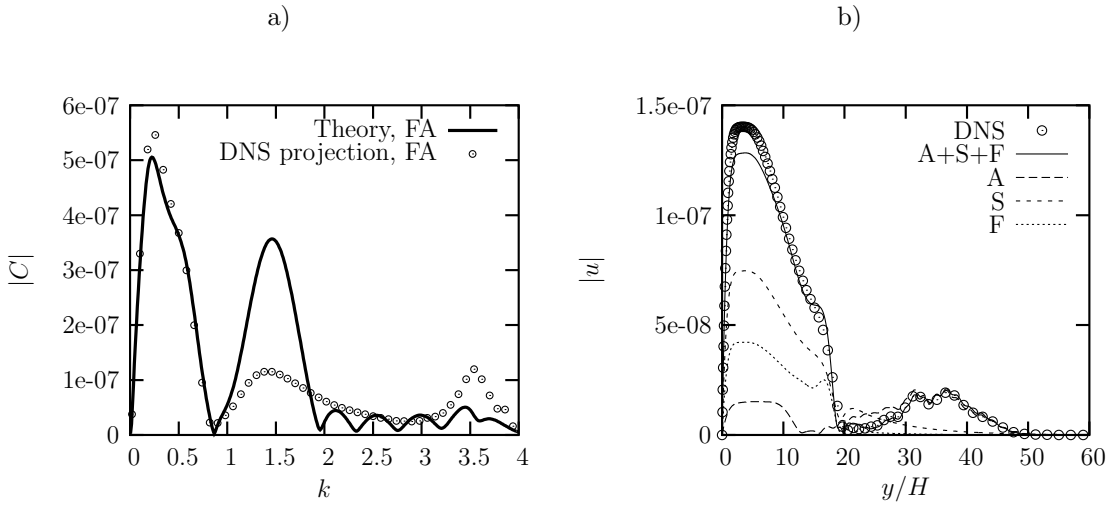

Figure 21. Amplitudes of the fast acoustic modes (a) and reconstructed velocity perturbation profiles (b), case 1 (193.96 kHz).

V. Discussion of the results

The results of the present work serve as an illustration of how the biorthogonal eigenfunction system can provide an insight into computational results. In order to be able to distinguish the modes, one needs amplitude and phase distributions for pressure, temperature, and velocity components, together with some of their derivatives given at only one station x. The necessary information is always available in computational studies, and the described method allows finding the amplitudes of the modes from the discrete and continuous spectra. For example, the results illustrate how one can find amplitudes of the decaying modes that could not be addressed at all in the past.

The solution in the present work is based on the parallel flow approximation. This approximation is valid when the characteristic scale of the perturbation (wave length) is much smaller than the characteristic scale of the unperturbed flow in the downstream direction. This condition is violated when the actuator is located close to the leading edge (see case 3 in §IV). Results of the present work are also based on the assumption that the denominator in (19) is not equal to zero. Fedorov and Khokhlov[15] showed that the denominator is equal to zero at the branching point of two discrete modes. In this case, the nonparallel flow effects are to be taken into account in order to resolve the singularity. Analysis of case 6 ($f \approx 104$ kHz) showed that the denominator tends to zero in the case of synchronism between the discrete mode and the continuous spectra. Therefore, an extension of the theoretical model of Ref. 17 to the case of continuous spectra is required.

Decomposition of perturbations when only partial information is available is an ill-posed problem. Nevertheless, it is still possible to analyze the flow field if some additional information about the data is available. Tumin *et al.*,[7] Tumin,[1] Gaydos and Tumin,[2] Gaydos,[18] and Tumin[3] discussed examples where the perturbations could be decomposed into the normal modes when only partial information was available. Further development of this approach might be especially helpful in analysis of experimental data in high-speed boundary layers.

Acknowledgments

This work was sponsored by the Air Force Office of Scientific Research, USAF, under grants No. FA9550-05-101 (A. Tumin) and FA9550-04-1-0029 (X. Zhong and X. Wang) monitored by Dr. J. D. Schmisseur. The views and conclusions contained herein are those of the authors and should not be interpreted as necessarily representing the official polices or endorsements, either expressed or implied, of the Air Force Office of Scientific Research or the U. S. Goverment.

References

[1]Tumin, A., "Multimode decomposition of spatially growing perturbations in a two-dimensional boundary layer," *Phys. Fluids*, Vol. 15, 2003, pp. 2525–2540.

[2]Guydos, P. and Tumin, A., "Multimode decomposition in compressible boundary layers," *AIAA J.*, Vol. 42, 2004, pp. 1115–1121.

[3]Tumin, A., "Three-dimensional spatial normal modes in compressible boundary layers," AIAA Paper 2006–1109, 2006.

[4]Tumin, A. and Reshotko, E., "The problem of boundary-layer flow encountering a three-dimensional hump revisited," AIAA Paper 2004–0101, 2004.

[5]Tumin, A. and Reshotko, E., "Receptivity of a boundary-layer flow to a three-dimensional hump at finite Reynolds numbers," *Phys. Fluids*, Vol. 17, No. 9, 2005, paper No. 094101.

[6]Tumin, A., "Receptivity of compressible boundary layers to three-dimensional wall perturbations," AIAA Paper 2006–1110, 2006.

[7]Tumin, A., Amitay, M., Cohen, J., and Zhou, M., "A normal multi-mode decomposition method for stability experiments," *Phys. Fluids*, Vol. 8, 1996, pp. 2777–2779.

[8]Wang, X. and Zhong, X., "Receptivity of a Mach 8.0 flow over a sharp wedge with half-angle 5.3° to wall blowing-suction," AIAA Paper 2005–5025, 2005.

[9]Zhong, X., "High-Order Finite-Difference Schemes for Numerical Simulation of Hypersonic Boundary-Layer Transition," *Journal of Computational Physics*, Vol. 144, 1998, pp. 662–709.

[10]Ashpis, D. and Reshotko, E., "The vibrating ribbon problem revisited," *J. Fluid Mech.*, Vol. 213, 1990, pp. 531–547.

[11]Balakumar, P. and Malik, M. R., "Discrete modes and continuous spectra in supersonic boundary layer," *J. Fluid Mech.*, Vol. 239, 1992, pp. 631–656.

[12]Tumin, A. M. and Fedorov, A. V., "Spatial growth of disturbances in a compressible boundary layer," *J. Appl. Mech. Tech. Phys.*, Vol. 24, 1983, pp. 548–554.

[13]Fedorov, A. and Tumin, A., "Initial-value problem for hypersonic boundary layer flows," *AIAA J.*, Vol. 41, 2003, pp. 379–389.

[14]Fedorov, A. V. and Khokhlov, A. P., "Mode switching in a supersonic boundary layer," *J. Appl. Mech. Tech. Phys.*, Vol. 32, 1991, pp. 831–836.

[15]Fedorov, A. V. and Khokhlov, A. P., "Prehistory of instability in a hypersonic boundary layer," *Theor. Comp. Fluid Dyn.*, Vol. 14, 2001, pp. 359–375.

[16]Ma, Y. and Zhong, X., "Receptivity of a supersonic boundary layer over a flat plate. Part 2: Receptivity to freestream sound," *J. Fluid Mech.*, Vol. 488, 2003, pp. 79–121.

[17]Fedorov, A. V. and Khokhlov, A. P., "Receptivity of hypersonic boundary layer to wall disturbances," *Theor. Comp. Fluid Dyn.*, Vol. 15, 2002, pp. 231–254.

[18]Guydos, P., "Analysis of small perturbations in compressible boundary layers," MS Thesis, The University of Arizona, 2004.